

Performance Bounds in Positioning with the VIVE Lighthouse System

Greiff, M.; Robertsson, A.; Berntorp, K.

TR2019-068 July 11, 2019

Abstract

The VIVE lighthouse system is evaluated for indoor positioning of micro unmanned aerial vehicles (MUAVs). A detailed mathematical analysis is provided, including a CramerRao bound derivation and performance analysis of the MUAV state estimate. The lighthouse measurements are fused with inertial measurements in a multiplicative extended Kalman filter (MEKF). We consider two implementations, one with and the other without nonlinear LS pre-filtering, and demonstrate both in a real-time implementation. The results indicate that subcentimeter accuracy in the MUAV positioning, rivalling the best positioning systems on the market at a comparatively low price.

International Conference on Information Fusion (FUSION)

This work may not be copied or reproduced in whole or in part for any commercial purpose. Permission to copy in whole or in part without payment of fee is granted for nonprofit educational and research purposes provided that all such whole or partial copies include the following: a notice that such copying is by permission of Mitsubishi Electric Research Laboratories, Inc.; an acknowledgment of the authors and individual contributions to the work; and all applicable portions of the copyright notice. Copying, reproduction, or republishing for any other purpose shall require a license with payment of fee to Mitsubishi Electric Research Laboratories, Inc. All rights reserved.

Performance Bounds in Positioning with the VIVE Lighthouse System*

1st Marcus Greiff

Department of Automatic Control
Lund University
Lund, Sweden
marcus.greiff@control.lth.se

2nd Anders Robertsson

Department of Automatic Control
Lund University
Lund, Sweden
anders.robertsson@control.lth.se

3rd Karl Berntorp

Department of Mechatronics
Mitsubishi Electric Research Laboratories
Cambridge, MA, US
karl.o.berntorp@ieee.org

Abstract—The VIVE lighthouse system is evaluated for indoor positioning of micro unmanned aerial vehicles (MUAVs). A detailed mathematical analysis is provided, including a Cramer-Rao bound derivation and performance analysis of the MUAV state estimate. The lighthouse measurements are fused with inertial measurements in a multiplicative extended Kalman filter (MEKF). We consider two implementations, one with and the other without nonlinear LS pre-filtering, and demonstrate both in a real-time implementation. The results indicate that sub-centimeter accuracy in the MUAV positioning, rivalling the best positioning systems on the market at a comparatively low price.

Index Terms—UAV positioning, nonlinear Kalman filtering

I. INTRODUCTION

Research on indoor positioning is a rich and cross-disciplinary field, motivated by its utility in practical applications and often driven by technological innovations. In this paper, we take a control-theoretic approach to the problem and restrict the scope to the positioning of multiple micro unmanned aerial vehicles (MUAVs), specifically the Crazyflie 2.0 [1], [2]. The objective is to enable complete autonomy in applications such as the inventorying of supermarkets, by having each MUAV run all computation on its own CPU, minimizing communication with the positioning system as a whole. We shall assume that the MUAV can take a maximum payload in the order of a few grams, with any additional load resulting in a significantly decreased flight-time, posing great restrictions on the sensory equipment that may be considered. We further require that solutions be practically implementable, both in terms of real-time compliance and a low monetary cost. Given this context, the HTC VIVE lighthouse positioning system (LHPS) [3] is explored, achieving accurate positioning by fusing the measurements with inertial measurement unit (IMU) measurements in a multiplicative extended Kalman filter (MEKF) [4], [5]. The main focus of this paper is on mathematically describing the LHPS in order to perform a general and qualitative evaluation of the system based on its

noise characteristics. The fusion with inertial measurements in a MEKF is then demonstrated as a proof of concept.

Notable contenders to the proposed LHPS approach are found in classical computer vision, where positioning is often made possible by optical-flow based methods with cameras mounted on the MUAV, or by feedback from a set of rigidly mounted cameras, see e.g., [6] and the references therein. The former methods tend to be scalable but become intractable considering the computational constraints of the MUAV, while the best static camera solutions offer sub-millimeter positioning at a much higher hardware cost. Other interesting alternatives include Ultra-Wideband (UWB) approaches, and specifically the time-difference-of-arrival (TDOA) method, which is scalable in the sense that many MUAVs can operate in the same system [7]. While more generally applicable and cheaper than the static camera systems, the positional accuracy of the state-of-the-art UWB positioning is in the multi-centimeter range [5], [8], [9].

It is clear that solutions to the indoor positioning problem generally trade scalability and accuracy for monetary cost and computational effort. This makes the considered LHPS a strong candidate in several respects. Firstly, the complete system is cheaper than both the high-performance static camera systems and the UWB systems, with a single lighthouse base station costing approximately \$130 [3]. Secondly, the LHPS is scalable with respect to the number of MUAVs that can operate simultaneously in the flyable space. Thirdly, the IR-diodes can be surface mounted on the MUAV, greatly reducing the payload and increasing flight-time. Fourthly, the processing of the measured signals can be made computationally cheap to a point where it may be done on the embedded system. Finally, the LHPS enables highly accurate positioning with standard deviations of the estimates in the millimeter range, as shown in the discussion of Section V.

In the field of UWB positioning, accuracy is often evaluated in terms of a Cramer-Rao bound (CRB) [2], [8]. The CRB is a theoretical lower bound of any unbiased parameter estimate by its relation to Fisher information, see e.g., [10], [11]. To evaluate the LHPS and properly compare it to UWB positioning, we first give a rigorous mathematical description of the positioning system in Section III, followed by a derivation of the measurement equations with an experimental charac-

*The research leading to these results has received funding from the Swedish Science Foundation (SSF) project "Semantic mapping and visual navigation for smart robots" (RIT15-0038). Dept. of Automatic Control, LTH, Lund University, SE-221 00 Lund, Sweden. The work was partially supported by the Wallenberg Artificial Intelligence, Autonomous Systems and Software Program (WASP) funded by Knut and Alice Wallenberg Foundation. The authors are members of the LCCC Linnaeus Center and the ELLIIT Excellence Center at Lund University.

terization of the stochastic noise in Section IV. An analysis is done by deriving the CRB for the LHPS in Section V, concluding sub-centimeter accuracy in the positional estimate in large regions of space. This statement is experimentally verified in Section VI. Finally, and a real-time example of MUAV positioning is given in Section VII, fusing the LHPS measurements with inertial measurements in a MEKF.

II. DEFINITIONS AND NOMENCLATURE

Throughout the document, vectors and matrices are written in bold font, letting $\mathbf{I}_N \in \mathbb{R}^{N \times N}$ denote the identity matrix, and $\mathbf{1}_N \in \mathbb{R}^{N \times N}$ denote a matrix with all elements set to one. The expectation, variance, standard deviation and covariance of a random variable, \mathbb{X} , are denoted with $\mathbb{E}[\mathbb{X}]$, $\mathbb{V}[\mathbb{X}]$, $\sigma(\mathbb{X})$, and $\mathbb{C}[\mathbb{X}]$, respectively. Indices of sets or vectors are defined using logical and (\wedge) and logical or (\vee) operators, such that in a set with three vectors, $\{\mathbf{a}_i\}_{i=1}^3 = \{\mathbf{a}_1, \mathbf{a}_2, \mathbf{a}_3\}$, reference to vectors $\mathbf{a}_2, \mathbf{a}_3 \in \{\mathbf{a}_i\}_{i=1}^3$ is written $\mathbf{a}_{2\vee 3}$, and the expectation of any of these vectors is written $\mathbb{E}[\mathbf{a}_{2\vee 3}]$. Furthermore, let \otimes denote the standard Kronecker product.

Let $\mathbf{p} \in \mathbb{R}^3$ be the MUAV position in a standard global orthonormal frame $\{\mathbf{e}_1, \mathbf{e}_2, \mathbf{e}_3\}$ with $\mathbf{e}_i \in \mathbb{R}^3$. Furthermore, let $\mathbf{v} \in \mathbb{R}^3$ be the velocity of the MUAV in the body frame of reference, defined by the orthonormal basis vectors $\{\mathbf{b}_1, \mathbf{b}_2, \mathbf{b}_3\}$ with $\mathbf{b}_i \in \mathbb{R}^3$. Let $\mathbf{R} \in SO(3)$ denote the rotation of a vector from this body frame to the global frame,

$$[\mathbf{e}_1 \ \mathbf{e}_2 \ \mathbf{e}_3] = \mathbf{R} [\mathbf{b}_1 \ \mathbf{b}_2 \ \mathbf{b}_3]. \quad (1)$$

For a vector $\mathbf{v} \in \mathbb{R}^3$ with elements v_i , we let

$$[v]_{\times} = \begin{bmatrix} 0 & -v_3 & v_2 \\ v_3 & 0 & -v_1 \\ -v_2 & v_1 & 0 \end{bmatrix} \quad (2)$$

and take $\boldsymbol{\omega} \in \mathbb{R}^3$ [rad] to be the attitude rate of the MUAV in the body frame, satisfying

$$\dot{\mathbf{R}}(t) = \mathbf{R}(t)[\boldsymbol{\omega}(t)]_{\times}. \quad (3)$$

Refer to [12]–[14] for details on attitude representations and identities related to the Lie algebra of the $SO(3)$ -manifold.

A. The Extended Kalman Filter Prediction Model

With the above definitions, the dynamics of the $SE(3)$ -configured MUAV is expressed in an attitude error form,

$$\begin{aligned} \dot{\boldsymbol{\rho}}(t) &= \boldsymbol{\omega}(t) + \frac{1}{2}[\boldsymbol{\rho}(t)]_{\times}\boldsymbol{\omega}(t), \\ \dot{\mathbf{p}}(t) &= \mathbf{R}(t)(\mathbf{I}_3 + [\boldsymbol{\rho}(t)]_{\times})\mathbf{v}(t), \\ \dot{\mathbf{v}}(t) &= \frac{f(t)}{m}\mathbf{e}_3 - [\boldsymbol{\omega}(t)]_{\times}\mathbf{v}(t) - g(\mathbf{I}_3 - [\boldsymbol{\rho}(t)]_{\times})\mathbf{R}(t)^T\mathbf{e}_3, \end{aligned} \quad (4)$$

where $f(t)/m$ [m/s²] denotes an acceleration generated by the rotors along \mathbf{b}_3 , g [m/s²] denotes the gravitational acceleration and $\boldsymbol{\rho}$ [rad] denotes an attitude error in the body frame [5]. Prior work on utilising this prediction model in a MEKF is found in [4], with details on the attitude-error in [12]. We refer to the deterministic prediction model of the MEKF in (4), by

$$\dot{\mathbf{x}}(t) = \mathbf{f}(\mathbf{x}(t), \mathbf{u}(t)) \in \mathbb{R}^9, \quad (5)$$

defining the corresponding control signal and state vector as

$$\mathbf{x} \triangleq [\mathbf{p}^T \ \mathbf{v}^T \ \boldsymbol{\rho}^T]^T \in \mathbb{R}^9, \quad \mathbf{u} \triangleq [f \ \boldsymbol{\omega}^T]^T \in \mathbb{R}^4. \quad (6)$$

The attitude-error relates to an element of $SO(3)$ by,

$$\delta\mathbf{R}\{\boldsymbol{\rho}\} \triangleq \mathbf{I}_3 + \frac{\sin(\beta)}{\beta}[\boldsymbol{\rho}]_{\times} + \frac{(1 - \cos(\beta))}{\beta^2}[\boldsymbol{\rho}]_{\times}^2,$$

denoting $\beta = \|\boldsymbol{\rho}\|_2$. In the MEKF proposed in [4], this attitude error-state is incorporated into the rotational estimate and reset to $\mathbf{0}$ only when it exceeds a bound in the l_1 -norm. The error is accumulated over a time-interval $[t_u, t]$, updating the rotational estimate by the rotational composition

$$\mathbf{R}(t) = \mathbf{R}(t_u) \cdot \delta\mathbf{R}\{\boldsymbol{\rho}(t)\}, \quad (7)$$

only when $\|\boldsymbol{\rho}\|_1 > c$ for some constant $c \approx 10^{-3}$ [rad]. A new update time $t_u = t$ is then set, and $\boldsymbol{\rho}(t_u) \triangleq \mathbf{0}$. As such, the length of the time interval $[t_u, t]$ varies depending on how much the MUAV is rotated. This idea may seem dubious, as the attitude error will be small at all times with its norm appearing in the denominator of both expressions. However,

$$\lim_{\beta \rightarrow 0} \frac{\sin(\beta/a)}{\beta} = \frac{1}{a}, \quad \lim_{\beta \rightarrow 0} \frac{1 - \cos(\beta)}{\beta^2} = \frac{1}{2}, \quad (8)$$

with $\delta\mathbf{R}\{\boldsymbol{\rho}\} \rightarrow \mathbf{I}_3$ as $\beta \rightarrow 0$, showing that the method is feasible even for small attitude-errors. Filters with such aperiodic updates come with many numerical benefits, but add complexity when deriving the associated measurement equations, as there only ever exists a relative attitude error-state in the MEKF. A central objective of this paper is therefore to express the measurements in the LHPS as a function of the $\mathbf{x}(t)$ for fusion in the MEKF in [5].

B. The Lighthouse Geometry

In the LHPS, a set of base stations emit light that is sensed by a set of mobile photodiodes mounted to the MUAVs, with the BWP34 IR-diodes used in the real-time implementation [15]. To define the LHPS geometry in relation to the MEKF prediction model, we give two definitions.

Definition 1: Let $\mathcal{S}^i, i \in \mathbb{N}$ denote an IR-sensor mounted rigidly at a position $\mathbf{p}_s^i \in \mathbb{R}^3$ in the MUAV body frame. The set of N sensors attached to the MUAV is denoted $\{\mathcal{S}^i\}_{i=1}^N$.

In the current hardware, a total of $N = 2$ sensors are implemented (see Fig. 1), but future revisions could include more sensors requiring sufficiently general definitions. The nominal LHPS configuration with two base stations depicted in Fig. 2 and explicitly stated in the Appendix.

Definition 2: Let $\mathcal{B}^j, j \in \mathbb{N}$, denote a base station, defined at a fixed point $\mathbf{p}_b^j \in \mathbb{R}^3$ in the global frame of reference. The fixed frame of the base \mathcal{B}^j is given by an orthonormal frame $\{\mathbf{b}_{1b}^j, \mathbf{b}_{2b}^j, \mathbf{b}_{3b}^j\}$, where similarly to the rotation in (1),

$$[\mathbf{e}_1 \ \mathbf{e}_2 \ \mathbf{e}_3] = \mathbf{R}_b^j [\mathbf{b}_{1b}^j \ \mathbf{b}_{2b}^j \ \mathbf{b}_{3b}^j].$$

The set of M base stations is denoted $\{\mathcal{B}^j\}_{j=1}^M$.

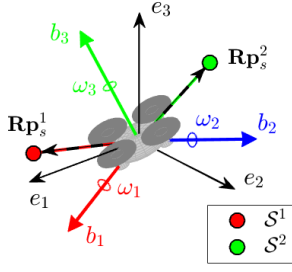


Fig. 1. A MUAV with two sensors $\{\mathcal{S}^i\}_{i=1}^2$ attached to the body frame.

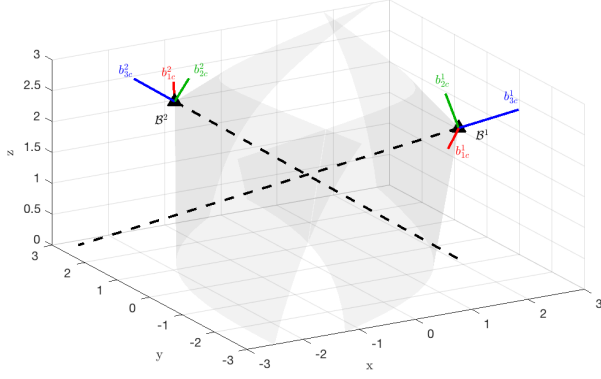


Fig. 2. Nominal system geometry with two base stations $\{\mathcal{B}^j\}_{j=1}^2$, and spaces \mathcal{X}^j depicting the flyable region in which the scanning planes exist.

III. THE VIVE LIGHTHOUSE SYSTEM

The lighthouse system functions much like a conventional lighthouse, in that it periodically sweeps planes of light over a space. The sweeps are done by multiple base stations, \mathcal{B}^j , located at known spatial positions, and the light is detected by a set of mobile BWP34 photodiodes [15], attached to the MUAVs as shown in Figure 1. In each base station, two spinning discs are equipped with wide-angle lasers situated on the two axis \mathbf{b}_{1b}^j and \mathbf{b}_{2b}^j . The discs spin with constant angular rates, effectively generating two half-planes of infrared light revolving around the corresponding axis at 120 [Hz], and each base station \mathcal{B}^j enables positioning in a half sphere, with a radius of approximately 5 [m].

Definition 3: Let \mathcal{B}^j be a base station and define

$$\mathcal{X}^j = \{x\mathbf{b}_{1c}^j + y\mathbf{b}_{2c}^j + z\mathbf{b}_{3c}^j \mid z < 0, x^2 + y^2 + z^2 \leq 5\},$$

as the space scanned by the lasers in the base station \mathcal{B}^j .

Definition 4: Let \mathcal{S}^i be a sensor and \mathcal{B}^j be a base station. Define two angles $\alpha_A^{ij}(t)$ and $\alpha_B^{ij}(t)$ [rad], where

$$\mathbf{n}_A^{ij}(t) = [\cos(\alpha_A^{ij}(t)) \quad 0 \quad -\sin(\alpha_A^{ij}(t))]^T \in \mathbb{R}^3, \quad (9a)$$

$$\mathbf{n}_B^{ij}(t) = [0 \quad \cos(\alpha_B^{ij}(t)) \quad \sin(\alpha_B^{ij}(t))]^T \in \mathbb{R}^3, \quad (9b)$$

denote the two normal vectors to each of the scanning planes in the frame $\{\mathbf{b}_{1b}^j, \mathbf{b}_{2b}^j, \mathbf{b}_{3b}^j\}$ associated with \mathcal{B}^j , such that

$$\begin{aligned} \Pi_A^{ij}(t) &= \{\mathbf{p} \in \mathbb{R}^3 \mid \mathbf{p}^T \mathbf{n}_A^{ij}(t) = 0, \mathbf{p} \cdot (\mathbf{n}_A^{ij}(t) \times \mathbf{b}_{1b}^j) \geq 0\}, \\ \Pi_B^{ij}(t) &= \{\mathbf{p} \in \mathbb{R}^3 \mid \mathbf{p}^T \mathbf{n}_B^{ij}(t) = 0, \mathbf{p} \cdot (\mathbf{n}_B^{ij}(t) \times \mathbf{b}_{2b}^j) \geq 0\}. \end{aligned}$$

Note here that by the mechanics in the LHPS, $\alpha_A^{ij}(t) = \alpha_B^{ij}(t) + \pi \forall t$. As such, the two planes in each \mathcal{B}^j satisfy

$$\Pi_A^{ij}(t) \cup \mathcal{X}^j \neq \emptyset \Rightarrow \Pi_B^{ij}(t) \cup \mathcal{X}^j = \emptyset,$$

$$\Pi_B^{ij}(t) \cup \mathcal{X}^j \neq \emptyset \Rightarrow \Pi_A^{ij}(t) \cup \mathcal{X}^j = \emptyset,$$

meaning that at most one of the two planes $\Pi_{AVB}^{ij}(t)$ exists in \mathcal{X}^j at any point in time.

A. The Single Lighthouse

The measurements taken in the mobile sensors are timer-based, measuring the time-delays between IR-pulses emitted from the base stations. To illustrate this, consider first a single lighthouse \mathcal{B}^j and a single sensor \mathcal{S}^i . In each state $\alpha_A^{ij}(t_0) = 2n\pi$, $n \in \mathbb{N}$, a relatively long pulse of light is emitted from the lighthouse in all of \mathcal{X}^j , lasting for $t_s^j \in [65, 135]$ [μ s]. Starting from t_0 , the plane Π_A^{ij} then sweeps over the entirety of \mathcal{X}^j during $t_\delta = 1/120$ [ms] rotating about \mathbf{b}_{1b}^j . If a sensor \mathcal{S}^i detects a short pulse of length $t_p^j \approx 10$ [μ s] at a time $t_A^{ij} \in [t_0, t_0 + t_\delta]$, then the angular state of the disc (A) at this time is $\alpha_A^{ij} = \pi(t_A - t_0)/t_\delta$. At $t_0 + t_\delta$, another synchronization flash is emitted indicating the start of a sweep Π_B^{ij} over \mathcal{X}^j . A short pulse is registered by the sensor at a time $t_B^{ij} \in [t_0 + t_\delta, t_0 + 2t_\delta]$, where then $\alpha_B^{ij} = \pi(t_B - t_0 + t_\delta)/t_\delta$, completing a full cycle of scans. When using a single base, \mathcal{B}^0 , with a single sensor, \mathcal{S}^X , a cycle of scans is done in measuring the two time-delays

$$\underbrace{t_s^0 \mid t_p^0}_{\alpha_A^{X0}} \mid \underbrace{t_s^0 \mid t_p^0}_{\alpha_B^{X0}}, \quad (10)$$

allowing for the computation of two angles $\{\alpha_A^{X0}, \alpha_B^{X0}\}$.

B. Multiple Lighthouses

When operating a set of two lighthouses, $\{\mathcal{B}^0, \mathcal{B}^1\}$, two synchronization flashes are done in quick succession before beginning a sweep, allowing the bases to coordinate their mechanical movement. Let $\{\mathcal{S}^X, \mathcal{S}^Y\}$ define two sensors. The sequence of flashes in the base stations is then,

$$\underbrace{t_s^0 \mid t_s^1 \mid t_p^0}_{\alpha_A^{X0}} \mid \underbrace{t_s^0 \mid t_s^1 \mid t_p^0}_{\alpha_B^{X0}} \mid \underbrace{t_s^0 \mid t_s^1 \mid t_p^1}_{\alpha_A^{X1}} \mid \underbrace{t_s^0 \mid t_s^1 \mid t_p^1}_{\alpha_B^{X1}}, \quad (11a)$$

$$\underbrace{t_s^0 \mid t_s^1 \mid t_p^0}_{\alpha_A^{Y0}} \mid \underbrace{t_s^0 \mid t_s^1 \mid t_p^0}_{\alpha_B^{Y0}} \mid \underbrace{t_s^0 \mid t_s^1 \mid t_p^1}_{\alpha_A^{Y1}} \mid \underbrace{t_s^0 \mid t_s^1 \mid t_p^1}_{\alpha_B^{Y1}}, \quad (11b)$$

which are measured in parallel in \mathcal{S}^X and \mathcal{S}^Y . Similarly to the single lighthouse, the sequences above allow for the computation of the angles defining plane normals. In this case, we get two sets of angles $\{\alpha_A^{X0}, \alpha_B^{X0}, \alpha_A^{X1}, \alpha_B^{X1}\}$ and $\{\alpha_A^{Y0}, \alpha_B^{Y0}, \alpha_A^{Y1}, \alpha_B^{Y1}\}$, one corresponding to each sensor. For simplicity, we consider the all measurements in the LHPS in terms of the plane angles, as opposed to the time-delays.

IV. MEASUREMENT EQUATIONS

To make use of the information contributed by the LHPS measurements, we first derive the associated equations in terms of the system state vector $\mathbf{x}(t)$ defined in (6). For the sake of generality, we consider a set of N sensors $\{\mathcal{S}^i\}_{i=1}^N$ and a set of M base stations $\{\mathcal{B}^j\}_{j=1}^M$. When processing the pulses emitted from the lighthouses measured by the sensors, we then compute a total of $2MN$ measured angles as,

$$\hat{\alpha}_{AVB}^{ij}(t) = \alpha_{AVB}^{ij}(\mathbf{x}(t)) + b_{AVB}^{ij}(t) + n_{AVB}^{ij}(t), \quad (12)$$

for some function $\alpha_{AVB}^{ij}(\mathbf{x}(t))$ of the system state, a bias term $b_{AVB}^{ij}(t)$ and stochastic noise $n_{AVB}^{ij}(t)$. The objective in this section is to characterize these functions, and verify any assumption with experimental data. We start with the angular function $\alpha_{AVB}^{ij}(\mathbf{x}(t))$ in Section IV-A, followed by the analytical expression of its Jacobians in Section IV-B and a characterisation of the stochastic noise in Section IV-C.

A. The Plane Angle Measurement Functions

To model the angles of the sweeping planes in terms of the state vector $\mathbf{x}(t)$, we utilize the attitude error-state as an incremental rotation. To recapitulate this idea, $\delta\mathbf{R}\{\boldsymbol{\rho}\}$ denotes an incremental rotation of the MUAV since last updating the rotational estimate at some time $t_u \leq t$. As such, the rotation at a time t becomes $\mathbf{R}(t) = \mathbf{R}(t_u)\delta\mathbf{R}\{\boldsymbol{\rho}(t)\}$. In the global frame, the vector from \mathcal{B}^j to a sensor \mathcal{S}^i is then

$$\mathbf{d}^{ij}(\mathbf{x}(t)) \triangleq \mathbf{p}(t) + \mathbf{R}(t)\mathbf{p}_s^i - \mathbf{p}_b^j \quad (13a)$$

$$= \mathbf{p}(t) + \mathbf{R}(t_u)\delta\mathbf{R}\{\boldsymbol{\rho}(t)\}\mathbf{p}_s^i - \mathbf{p}_b^j, \quad (13b)$$

which, when normalized, yields a ray vector,

$$\mathbf{r}^{ij}(\mathbf{x}) \triangleq \mathbf{d}^{ij}(\mathbf{x})/\|\mathbf{d}^{ij}(\mathbf{x})\|_2. \quad (14)$$

The normal of the corresponding plane is then given by

$$\mathbf{n}_A^{ij}(\mathbf{x}) = (\mathbf{r}^{ij}(\mathbf{x}) \times \mathbf{b}_{1b}^j) = -[\mathbf{b}_{1b}^j]_{\times} \mathbf{r}^{ij}(\mathbf{x}), \quad (15a)$$

$$\mathbf{n}_B^{ij}(\mathbf{x}) = (\mathbf{r}^{ij}(\mathbf{x}) \times \mathbf{b}_{2b}^j) = -[\mathbf{b}_{2b}^j]_{\times} \mathbf{r}^{ij}(\mathbf{x}). \quad (15b)$$

To proceed, we define an intermediary function

$$g_A^{ij}(\mathbf{x}) = \mathbf{e}_1^T \mathbf{n}_A^{ij}(\mathbf{x}), \quad g_B^{ij}(\mathbf{x}) = \mathbf{e}_2^T \mathbf{n}_B^{ij}(\mathbf{x}), \quad (16a)$$

which notably differs in the A and B angle cases. Finally, we write the angles from the definition of the plane normals (9),

$$\alpha_A^{ij}(\mathbf{x}) = \arccos(g_A^{ij}(\mathbf{x})), \quad \alpha_B^{ij}(\mathbf{x}) = \arccos(g_B^{ij}(\mathbf{x})), \quad (17a)$$

with two different functions for the A and B cases, which exist for all $\mathbf{d}^{ij}(\mathbf{x}) \neq \mathbf{0}$.

B. The Plane Angle Measurement Jacobians

The obtained expression of the angular measurements allows for the analytical derivation of the Jacobian with respect to the state vector $\mathbf{x}(t) = [\mathbf{p}(t) \quad \mathbf{v}(t) \quad \boldsymbol{\rho}(t)]$, defined in (6). This is central to the measurement updates in the MEKF and

later derivations of the Cramer-Rao Bound. Starting by differentiating with respect to the position, \mathbf{p} , using the function definitions in Section IV-A and applying the chain rule yields

$$\frac{\partial \alpha_A^{ij}}{\partial \mathbf{p}} = \frac{\partial \alpha_A^{ij}}{\partial g_A^{ij}} \cdot \frac{\partial g_A^{ij}}{\partial \mathbf{n}_A^{ij}} \cdot \frac{\partial \mathbf{n}_A^{ij}}{\partial \mathbf{r}^{ij}} \cdot \frac{\partial \mathbf{r}^{ij}}{\partial \mathbf{d}^{ij}} \cdot \frac{\partial \mathbf{d}^{ij}}{\partial \mathbf{p}} \in \mathbb{R}^{1 \times 3}. \quad (18)$$

Computing these partial derivatives, we find that

$$\frac{\partial \alpha_A^{ij}}{\partial \mathbf{p}} = \frac{\mathbf{e}_1^T [\mathbf{b}_{1b}^j]_{\times}}{\sqrt{1 - (g_A^{ij})^2}} \frac{[(\mathbf{d}^{ij})^T \mathbf{d}^{ij}] \mathbf{I}_3 - \mathbf{d}^{ij} (\mathbf{d}^{ij})^T}{[(\mathbf{d}^{ij})^T \mathbf{d}^{ij}]^{3/2}}, \quad (19a)$$

$$\frac{\partial \alpha_B^{ij}}{\partial \mathbf{p}} = \frac{\mathbf{e}_2^T [\mathbf{b}_{2b}^j]_{\times}}{\sqrt{1 - (g_B^{ij})^2}} \frac{[(\mathbf{d}^{ij})^T \mathbf{d}^{ij}] \mathbf{I}_3 - \mathbf{d}^{ij} (\mathbf{d}^{ij})^T}{[(\mathbf{d}^{ij})^T \mathbf{d}^{ij}]^{3/2}}. \quad (19b)$$

As $\alpha_{AVB}^{ij}(\mathbf{x})$ is independent of the velocity $\mathbf{v}(t)$,

$$\frac{\partial \alpha_{AVB}^{ij}}{\partial \mathbf{v}} = \mathbf{0} \in \mathbb{R}^{1 \times 3} \quad \forall i, j. \quad (20)$$

Finally, we consider the rotation in terms of the attitude error,

$$\frac{\partial \mathbf{d}^{ij}}{\partial \boldsymbol{\rho}} = \frac{\partial \mathbf{R}\{\boldsymbol{\rho}\} \mathbf{p}_s^i}{\partial \boldsymbol{\rho}} = -\mathbf{R}(\delta\mathbf{R}\{\boldsymbol{\rho}\} [\mathbf{p}_s^i]_{\times}) J(\boldsymbol{\rho}) \triangleq \tilde{J}(\boldsymbol{\rho}), \quad (21)$$

where

$$\mathbf{J}(\boldsymbol{\theta}) = \mathbf{I}_3 - \frac{1 - \cos(\|\boldsymbol{\theta}\|_2)}{\|\boldsymbol{\theta}\|_2} [\boldsymbol{\theta}]_{\times} + \frac{\|\boldsymbol{\theta}\|_2 - \cos(\|\boldsymbol{\theta}\|_2)}{\|\boldsymbol{\theta}\|_2^3} [\boldsymbol{\theta}]_{\times}^2, \quad (22)$$

as shown in [16]. Application of the chain rule as in (18) yields

$$\frac{\partial \alpha_A^{ij}}{\partial \boldsymbol{\rho}} = \frac{\mathbf{e}_1^T [\mathbf{b}_{1b}^j]_{\times}}{\sqrt{1 - (g_A^{ij})^2}} \frac{[(\mathbf{d}^{ij})^T \mathbf{d}^{ij}] \mathbf{I}_3 - \mathbf{d}^{ij} (\mathbf{d}^{ij})^T}{[(\mathbf{d}^{ij})^T \mathbf{d}^{ij}]^{3/2}} \tilde{J}(\boldsymbol{\rho}), \quad (23a)$$

$$\frac{\partial \alpha_B^{ij}}{\partial \boldsymbol{\rho}} = \frac{\mathbf{e}_2^T [\mathbf{b}_{2b}^j]_{\times}}{\sqrt{1 - (g_B^{ij})^2}} \frac{[(\mathbf{d}^{ij})^T \mathbf{d}^{ij}] \mathbf{I}_3 - \mathbf{d}^{ij} (\mathbf{d}^{ij})^T}{[(\mathbf{d}^{ij})^T \mathbf{d}^{ij}]^{3/2}} \tilde{J}(\boldsymbol{\rho}). \quad (23b)$$

We have then managed to model the angle $\alpha_{AVB}^{ij}(\mathbf{x})$ associated with each plane $\Pi_{AVB}^{ij}(t)$ for any sensor \mathcal{S}^j when receiving a sweep from a base station \mathcal{B}^j . We have also expressed the Jacobian of this function with respect to the state $\mathbf{x}(t)$ in equations (19a), (19b), (20), (23a) and (23b).

C. The Plane Angle Measurement Noise

To investigate the stochastic noise $n_{AVB}^{ij}(t)$ in the measurement equation (12), a set of 80 measurement sets were taken with two sensors \mathcal{S}^i with $i \in [X, Y]$ and two base stations \mathcal{B}^j with $j \in [1, 2]$ in the nominal system configuration depicted in Figure 2. The sensors were placed 0.04 [m] apart and at random locations $\mathbf{p}_k \in \mathcal{X}^1 \cup \mathcal{X}^2$ with $k \in [1, \dots, 80]$. A total of 10^3 samples of $\hat{\alpha}_{AVB}^{ij}$ were taken in each set, referred to by $\mathcal{D}(A \vee B, i, j, k)$. The sets are visualized in Figure 3 with two sample sets, one representing a typical inlier set $\mathcal{D}(A, X, 2, 2)$ (red) and one a typical outlier set $\mathcal{D}(A, X, 1, 4)$ (blue). In addition, the logarithmic standard

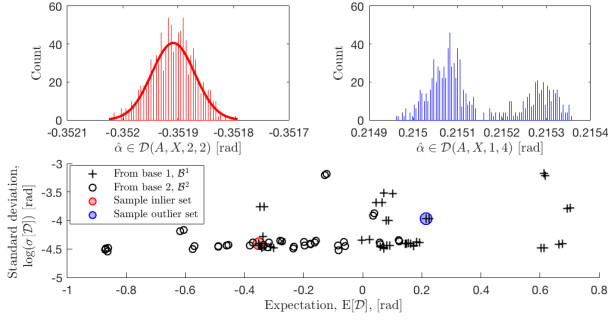


Fig. 3. *Top Left*: The distribution of the measurements in the inlier set, $\mathcal{D}(A, X, 2, 2)$, with a scaled Gaussian density function. *Top Right*: The distribution of the measurements in the sample the outlier set $\mathcal{D}(A, X, 1, 4)$. *Bottom*: Logarithmic standard deviation of \mathcal{D} as a function of its mean.

deviation $\log(\sigma[\mathcal{D}])$ is plotted against $\mathbb{E}[\mathcal{D}]$, with the two sample sets highlighted.

The standard deviation of the angular measurement noise approaches $\sigma[\mathcal{D}] \approx 10^{-4.5}$ [rad] in a vast majority of the measurement sets, exemplified by a sample inlier measurement set (red). There are, however, some outlier sets, which have an interesting structure with distinct multimodal distributions (blue) where $\sigma[\mathcal{D}] \in [10^{-4}, 10^{-3}]$ [rad]. Note that the standard deviation of the two peaks in the outlier set corresponds to that of the inlier set. This is the result of a discrete jump in the measurement mean, made visible when showing angular measurements of the outlier set in Figure 4.

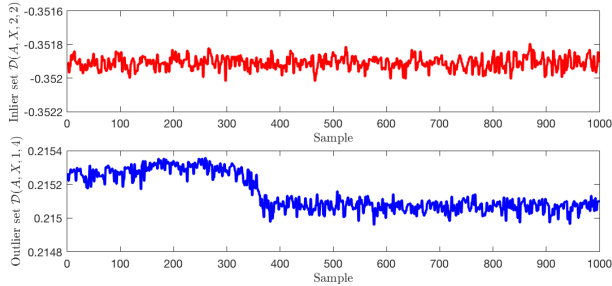


Fig. 4. *Top*: The sample inlier set of angular measurements, $\mathcal{D}(A, X, 2, 2)$. *Bottom*: The sample outlier set of angular measurements, $\mathcal{D}(A, X, 1, 4)$.

It is clear that the angular measurement expectation makes a discrete jump at a singular point in time in the outlier sequence, an odd behaviour which cannot be attributed to the geometry of the room. We also note that all measurement sequences come in pairs in Figure 3, in the sense that measurement sets of the same angle from the two sensors will be strongly correlated, both for inlier sequences and outlier sequences. This is clearly demonstrated by studying the covariance of the inlier and outlier sets at a fixed position in the room, plotted in for position \mathbf{p}_2 and \mathbf{p}_4 in Figure 5). In the first plot, all eight measurement series qualify as inlier sequences, with unimodal distributions at $\sigma[\mathcal{D}] < 10^{-4}$. In the second plot, taken in \mathbf{p}_4 , only the sets $\mathcal{D}(A, X \vee Y, 1, 4)$ qualify as outlier sequences of which one, is depicted in Figure 4.

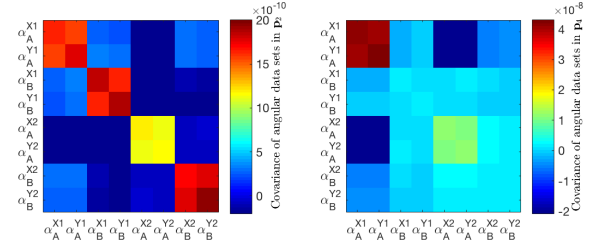


Fig. 5. *Left*: Covariance of measurements at a fixed position in the room where no outlier sets appear. *Right*: Covariance of measurements at a fixed position in the room where two significant outlier sets are present.

This illustrates the odd nature of the outlier sets, where small shifts in the expectation of the angular measurements seen in Figure 4, taken of the same angle from the same base station occur simultaneously and independently in both sensors. A plausible explanation for this phenomenon is the internal control of the discs in the base stations of the LHPS, accounting for the systematic and very small timing errors in the measurements of single angles in the base station.

From these experiments, we conclude that angular measurements are locally approximately Gaussian in their distribution with a standard deviation of $\sigma[\mathcal{D}] \approx 10^{-4.5}$ [rad] corresponding to a variance of $\mathbb{V}[\mathcal{D}] = 10^{-9}$, with the same cross-correlation for measurements of the same planar angle in different sensors. Furthermore, no significant correlation was found between the noise distribution and the spatial position of the sensor in $\mathcal{X}^1 \cup \mathcal{X}^2$. As seen in Figure 4, there exists a time-varying bias term which may be modeled in the MEKF with an additional two states per base station, as the same bias affects measurements of the same angle in the same base station taken by different sensors. To summarise, the noise is approximately Gaussian, and a small time-varying bias exists, which can be assumed identical over all sensors, and could be modeled as a first-order Markov process in the MEKF. However, we stress that the bias terms are small, being in the order of 10^{-3} [rad] corresponding the maximum distance between the multimodal peaks in the outlier data sets.

V. THE CRAMER-RAO LOWER BOUND

With the measurement equations modeled and experimentally verified, we may assess the informational content of LHPS measurements. Consider an unknown parameter vector consisting of the MUAV position and rotational attitude error,

$$\boldsymbol{\theta} = [\theta_1 \ \theta_2 \ \theta_3 \ \theta_4 \ \theta_5 \ \theta_6]^T \triangleq [\mathbf{p}^T \ \boldsymbol{\rho}^T]^T \in \mathbb{R}^6,$$

which is to be estimated by a set of measured angles relative to M base stations $\{\mathcal{B}^j\}_{j=1}^M$ sensed by N sensors $\{\mathcal{S}^i\}_{i=1}^N$. The reason for not including the velocity is that instantaneous measurements of the LHPS do not contribute any velocity information. Consequently, we start by forming a vector of all measurements taken at a singular point in time,

$$\hat{\boldsymbol{\alpha}} \triangleq \left[\hat{\alpha}_A^{11} \ \hat{\alpha}_A^{21} \ \dots \ \hat{\alpha}_B^{(N-1)M} \ \hat{\alpha}_B^{NM} \right]^T \in \mathbb{R}^{2NM},$$

partitioned such that all the measurement of the same angle in the same base station from every sensor appears in sets of N measurements, similar to the structure of the measurements in Figure 5. From the discussion in Section IV-C, the vector of measurements can be seen as random variable with a multivariate Gaussian distribution, with expectation

$$\boldsymbol{\mu}(\boldsymbol{\theta}) \triangleq [\alpha_A^{11}(\mathbf{x}) \quad \cdots \quad \alpha_B^{NM}(\mathbf{x})]^T \in \mathbb{R}^{2NM},$$

as derived in Section IV-A. Furthermore, the covariance of the stochastic noise was shown to be independent of $\boldsymbol{\theta}$, and may therefore be defined with the Kronecker product as

$$\mathbf{Q}(\boldsymbol{\theta}) = 10^{-9} \cdot (\mathbf{I}_{2M} \otimes \mathbf{1}_N) \in \mathbb{R}^{2NM \times 2NM},$$

by the discussion in Section IV-C. Consequently, we have

$$\hat{\boldsymbol{\alpha}} \sim \mathcal{N}(\boldsymbol{\mu}(\boldsymbol{\theta}), \mathbf{Q}(\boldsymbol{\theta})), \quad (24)$$

with a corresponding probability density function

$$p(\boldsymbol{\alpha}|\boldsymbol{\theta}) = \frac{\exp\left(-\frac{1}{2}(\boldsymbol{\alpha} - \boldsymbol{\mu}(\boldsymbol{\theta}))^T \mathbf{Q}^{-1}(\boldsymbol{\theta})(\boldsymbol{\alpha} - \boldsymbol{\mu}(\boldsymbol{\theta}))\right)}{\sqrt{(2\pi)^{2NM} |\mathbf{Q}(\boldsymbol{\theta})|}}, \quad (25)$$

if taking the angular bias in (12) to be zero. We may then find a simple formula for the computation of the Fisher information matrix (FIM), denoted $\mathcal{I}(\boldsymbol{\theta})$ [10].

Proposition 1: An element of the FIM at a row k and column l when taking N_s independent samples from the multivariate Gaussian distribution in (24) is given by

$$\begin{aligned} \mathcal{I}_{kl}(\boldsymbol{\theta}) &= \mathbb{E} \left[\frac{\partial \log p(\boldsymbol{\alpha}|\boldsymbol{\theta})}{\partial \theta_k} \frac{\partial \log p(\boldsymbol{\alpha}|\boldsymbol{\theta})}{\partial \theta_l} \right] \\ &= 2 \sum_{t=1}^{N_s} \frac{\partial \boldsymbol{\mu}^T(\boldsymbol{\theta})}{\partial \theta_k} \mathbf{Q}^{-1}(\boldsymbol{\theta}) \frac{\partial \boldsymbol{\mu}(\boldsymbol{\theta})}{\partial \theta_l} \\ &\quad + N_s \operatorname{tr} \left(\mathbf{Q}^{-1}(\boldsymbol{\theta}) \frac{\partial \mathbf{Q}(\boldsymbol{\theta})}{\partial \theta_k} \mathbf{Q}^{-1}(\boldsymbol{\theta}) \frac{\partial \mathbf{Q}(\boldsymbol{\theta})}{\partial \theta_l} \right), \end{aligned} \quad (26)$$

provided the Fisher information is always defined and the density function $p(\boldsymbol{\alpha}|\boldsymbol{\theta})$ in (25) has bounded support in $\boldsymbol{\alpha}$.

Proof 1: The result follows immediately from the definition of the FIM and insertion of the density function in (24). The complete proof is given in Appendix 3C in [10].

Corollary 1: In the event of parameter independence in $\mathbf{Q}(\boldsymbol{\theta})$, the second term in (26) vanishes, and the Jacobians in the first term, $\partial \boldsymbol{\mu}(\boldsymbol{\theta})/\partial \theta_i$, $i \in [1, 6]$, are given explicitly in equations (19a), (19a), (23a), and (23b) in Section IV-B.

The well known CRB of the estimate covariance, see e.g., [10], is then given by the inverse of the FIM as,

$$\mathbb{E}[(\boldsymbol{\theta} - \hat{\boldsymbol{\theta}})(\boldsymbol{\theta} - \hat{\boldsymbol{\theta}})^T] \geq \mathcal{I}^{-1}(\boldsymbol{\theta}). \quad (27)$$

To exemplify this bound, consider the nominal base station configuration in Figure 2 with a single sensor and an unknown parameter consisting of its positional estimate $\hat{\mathbf{p}} = [\hat{\theta}_1, \hat{\theta}_2, \hat{\theta}_3]$. Taking the FIM with $N_s = 1$ and $k, l \in \{1, 2, 3\}$, the CRB can be evaluated as a function of the position in a given problem geometry. The logarithmic trace of the CRB,

$$\min \log(\operatorname{tr}(\mathbb{E}[(\mathbf{p} - \hat{\mathbf{p}})(\mathbf{p} - \hat{\mathbf{p}})^T])), \quad (28)$$

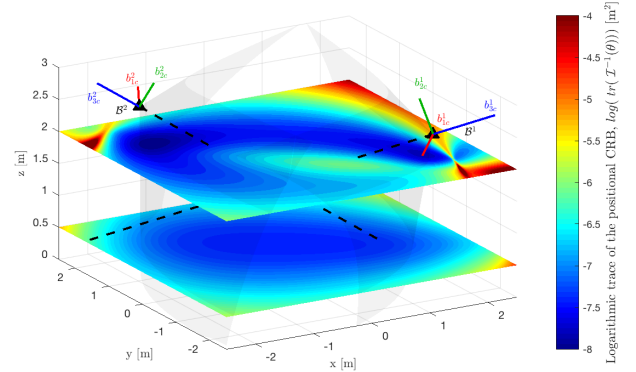


Fig. 6. Bound of the positional estimate covariance, with the logarithm of the CRB trace as a function of a spatial position in two $z_{e3} = 0.5$ and $z_{e3} = 2$.

is shown in Figure 6 in the planes $z_{e3} = 0.5$ and $z_{e3} = 2$.

Based on this result, two observations can be made. Firstly, there is a significant portion of the flyable space in which the logarithmic trace of the positional estimate covariance matrix approaches -8 , corresponding to a standard deviation of any positional estimate in the sub-millimeter range. This applies only under the assumption of the bias terms being perfectly estimated or zero at all times, but is still notably lower than the multi-centimeter standard deviation in modern UWB positioning [5], [9]. We also note a rapid growth in the CRB when approaching the line intersecting the positions of \mathbf{p}_b^1 and \mathbf{p}_b^2 of the two base stations. This is readily seen in the $z_{e3} = 2$, plane and conforms nicely with intuition, as angular measurements alone in a two-base station case cannot determine where on the line the MUAV is positioned. As such, there will exist an eigenvalue of the FIM approaching zero, where then $\min \log(\operatorname{tr}(\mathbb{E}[(\mathbf{p} - \hat{\mathbf{p}})(\mathbf{p} - \hat{\mathbf{p}})^T])) \rightarrow \infty$.

VI. NONLINEAR LEAST-SQUARES FILTERING

To show the theoretical CRB in practice, a least-squares (LS) algorithm is derived to estimate the position of a single sensor \mathcal{S}^i based on the $2M$ angular measurements from M base stations $\{\mathcal{B}^j\}_{j=1}^M$. Consider two angular measurements, $\hat{\alpha}_{A \wedge B}^{ij}$, taken from the same base station, \mathcal{B}^j . By the orthogonality of the plane normals defined in (9), the line in the intersection of these planes is given by a direction

$$\mathbf{r}^{ij} = \mathbf{R}_b^j (\mathbf{n}_A^{ij}(\hat{\alpha}_A^{ij}) \times \mathbf{n}_B^{ij}(\hat{\alpha}_B^{ij})), \quad (29)$$

resulting in the line $\mathbf{l}^{ij} = \mathbf{p}_b^j + \lambda \mathbf{r}^{ij}$ in the global frame, for some $\lambda \in \mathbb{R}$. With the angular measurements transformed into M lines, it is then possible to estimate the sensor position \mathbf{s}^i in the global frame. The closest distance squared between the desired point \mathbf{s}^i and a line \mathbf{l}^{ij} may be written in terms of the idempotent projector $\mathbf{P}^{ij} = \mathbf{I}^{ij} - \mathbf{r}^{ij}(\mathbf{r}^{ij})^T$, satisfying $(\mathbf{P}^{ij})^2 = \mathbf{P}^{ij}$. We then attempt to minimize a quadratic distance $\|\mathbf{s}^i - \mathbf{l}^j\|_2^2$ for every measured line, similar to the approach in [2], resulting in an LS-problem with a cost

$$J(\mathbf{s}^i) = \sum_{j=1}^M \|\mathbf{s}^i - \mathbf{l}^{ij}\|_2^2 = \sum_{j=1}^M (\mathbf{p}_b^j - \mathbf{s}^i)^T \mathbf{P}^{ij} (\mathbf{p}_b^j - \mathbf{s}^i). \quad (30)$$

The optimal estimate, $\hat{\mathbf{s}}^i$, with respect to minimizing (30) is

$$\hat{\mathbf{s}}^i = \arg \min_{\mathbf{s}^i} \|\mathbf{A}\mathbf{s}^i - \mathbf{b}\|_2^2 = (\mathbf{A}^T \mathbf{A})^{-1} (\mathbf{A}^T \mathbf{b}), \quad (31)$$

where

$$\mathbf{A} \triangleq \sum_{j=1}^M \mathbf{P}^{ij}, \quad \mathbf{b} \triangleq \sum_{j=1}^M \mathbf{P}^{ij} \mathbf{p}_b^j. \quad (32)$$

To test the accuracy of the derived LS filtering and relate it to the previous result on the CRB, an experiment was done with the nominal base station configuration in Figure 2. The positions of two sensors \mathcal{S}^1 (blue) and \mathcal{S}^2 (red) respectively were estimated independently online by (31). The sensors were mounted precisely 0.04 [m] apart at all times, and the result the result depicted in (see Figure 7).

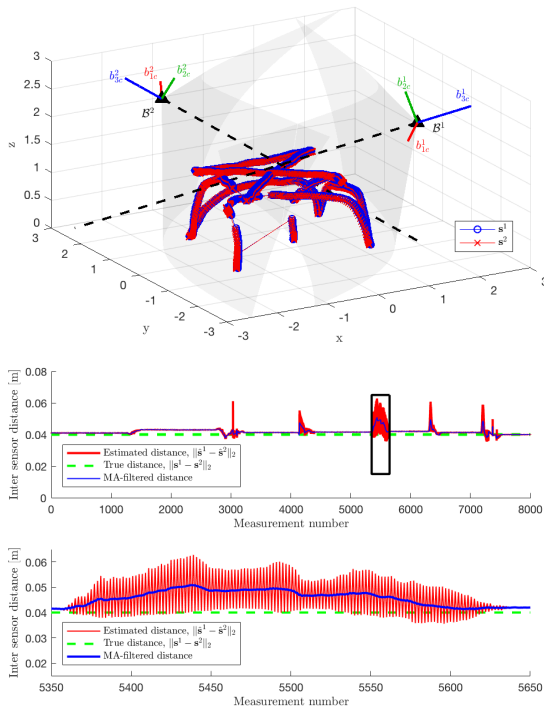


Fig. 7. *Top*: The positional trajectories of the two sensors, discrete jumps in measurements are caused by outlier rejection during occlusion. *Bottom*: Estimated inter-sensor distances (red), and MA-filtered estimates (blue), zoomed in on a volatile segment during movement (black box).

With this relatively simple form of filtering, we note that the independently estimated sensors are indeed approximately 0.04 [m] apart at all times, especially when the sensors are laying still. When manually moving the sensors in the room, there is a clear deterioration in positional estimates, as seen in the second plot of Figure 7, where the estimated distance (red) jumps back and forth between two points around a moderately varying mean (blue). The explanation for this behaviour lies in the way in which the LHPS-angles are computed. There is a time-delay of approximately 1/60 [s] between the angle computations in the two base stations, by virtue of the way in which the base stations synchronise the plane sweeps as

discussed in Section III. Consequently, the two lines in the LS-regression are never computed simultaneously, resulting in the distance between the sensors exhibiting a zing-zagging behaviour which is easily remedied by averaging the two most recent estimates in a moving average (MA) filter (blue).

The LS-filtering has some interesting connections to the CRB analysis in Section V. When the MUAV is laying still in an approximate position,

$$\mathbf{s}^1 \approx [0.122, 0.125, 0.813], \quad \mathbf{s}^2 \approx [0.116, 0.085, 0.813]$$

over approximately 20 seconds, we compute the logarithm of the trace of the covariance of the LS-estimated positions,

$$\log(\text{tr}(\mathbb{C}[\hat{\mathbf{s}}^1])) = -7.408, \quad \log(\text{tr}(\mathbb{C}[\hat{\mathbf{s}}^2])) = -7.364,$$

which is close to, but greater than the theoretical CRB at the corresponding points, computed as

$$\log(\text{tr}(\mathcal{I}^{-1}[\mathbf{s}^1])) = -7.536, \quad \log(\text{tr}(\mathcal{I}^{-1}[\mathbf{s}^2])) = -7.534.$$

In addition, the observation that the inverse FIM blows up as the MUAV resides on the line intersecting the position of both base stations is also nicely in the LS filtering, where it was shown that two parallel lines $\mathbf{I}^{i1} \|\mathbf{I}^{i2}$ result in a zero-eigenvalue in the idempotent operator \mathbf{P}^{ij} , and a blow up of the positional estimates. With two base stations, this is only possible if \mathbf{I}^{i1} and \mathbf{I}^{i2} both intersect the positions \mathbf{p}_b^1 and \mathbf{p}_b^2 , concurring with the observations made in Section V.

VII. FUSION WITH IMU-DATA IN THE MEKF

We now have two options when considering the fusion of IMU-data with the LHPS data in the MEKF. The first is to model the measurement using an MA-filtered LS-estimate of the MUAV position, implementing the measurement equation

$$\mathbf{y}_{LS}(t) = \mathbf{h}_{LS}(\mathbf{x}) = \mathbf{p}(t) + \mathbf{e}_{LS}(t) \in \mathbb{R}^3, \quad (33)$$

with $\mathbf{e}_{LS} \sim \mathcal{N}(\mathbf{0}, \mathbb{C}[\hat{\mathbf{s}}_i])$ and a corresponding Jacobian

$$\frac{\partial \mathbf{h}_{LS}(\mathbf{x})}{\partial \mathbf{x}} = [\mathbf{I}_3 \quad \mathbf{0}_3 \quad \mathbf{0}_3] \in \mathbb{R}^{3 \times 9}, \quad (34)$$

where measurement updates are done each time a full set of plane measurements are taken from each base station. This amounts to an update rate of approximately 30 [Hz] of the positional information, and sensitivity to outliers as an entire set of inlier angles needs to be retrieved from a base station before making a positional measurement update.

The second option is to implement the plane angle measurement equation in (12), and use this equation directly in the measurement update of the MEKF. This is appealing as new measurements are included at 120 [Hz] instead of 30 [Hz] in the LS case, and any inlier angle may be incorporated directly into the MEKF even if the second measured angle from the same base station is an outlier measurement. We assume a zero bias in the angles, and use a scalar equation

$$y_{\Pi}(t) = h_{\Pi}(\mathbf{x}) = \alpha_{AVB}^{ij}(\mathbf{x}) + n_{AVB}^{ij} \in \mathbb{R}, \quad (35)$$

as was derived in Section IV, with the corresponding Jacobian

$$\frac{\partial h_{\Pi}(\mathbf{x})}{\partial \mathbf{x}} = \begin{bmatrix} \frac{\partial \alpha_{AVB}^{ij}(\mathbf{x})}{\partial \mathbf{p}} & \mathbf{0}_{3 \times 1} & \frac{\partial \alpha_{AVB}^{ij}(\mathbf{x})}{\partial \boldsymbol{\rho}} \end{bmatrix} \in \mathbb{R}^{1 \times 9}. \quad (36)$$

We refer to [4], [5] for additional details on the MEKF, but the resulting positioning when implementing the direct plane measurements is shown in Figure 8, including the positional trajectory with simultaneous LS estimate done on-line, and the estimated attitude as extrinsic ZYX Tait-Bryan angles.

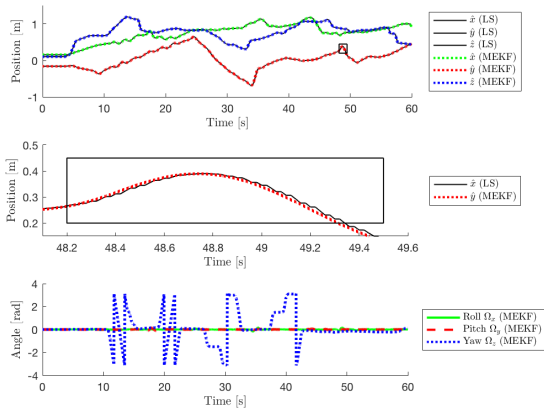


Fig. 8. A joystick controlled flight with LS-estimates and direct plane MEKF-estimates estimates logged during the flight. *Top*: Positional trajectory. *Center*: Zoomed in positional trajectory on \hat{y} during $t \in [48.2, 49.5]$ (black box). *Bottom*: Rotational trajectory in the extrinsic ZYX Tait-Bryan angles.

From this experiment, we note that the performance is very similar in the LS and MEKF cases, but the jagged estimate of the LS-scheme is clearly visible when zooming in on the state trajectory. While the LHPS is accurate to a point where the LS-estimates can be used directly in the feedback loop, the MEKF should always be considered, with or without LS pre-filtering, due to its robustness to temporary occlusion.

VIII. CONCLUSION

In this paper, the HTC VIVE Lighthouse system has been evaluated for MUAV positioning. The CRB of the MUAV state estimate was derived based on the LHPS measurement equations and the noise characteristics of the measured signals. This bound was subsequently experimentally validated by comparison to the covariance of the positional estimates of two different sensors at known locations in space. In all tested cases, the covariance was lower bound by the CRB, corresponding to a standard deviation of the positional estimates in millimetre range. We further illustrated the quality of the positional information by independently estimating the location of two sensors at a fixed positional offset, as mounted on the MUAV, recovering the true estimated inter-sensor distance with millimetre precision at various locations in the flyable space. Finally, we demonstrated two ways of fusing LHPS measurements with IMU-data in a MEKF running on the MUAV; the first using the LS pre-filtering on a set of four angular measurements in (33) and (34), and the second using

the angular measurement equations directly by (35) and (36). In conclusion, the LHPS is an accurate alternative to classical camera- and radio-based positioning systems in the same price range. Future work will explore alternative algorithms to the MEKF and the usage of more than two base stations.

IX. ACKNOWLEDGMENT

The authors would like to thank Arnaud Taffanel and Tobias Antonsson of Bitcraze AB for inspiration and generous help with technical details in the real-time implementation.

APPENDIX

The nominal configuration of the LHPS is given by

$$\mathbf{p}_b^j = \begin{bmatrix} 1.5769 \\ -1.6014 \\ 2.4486 \end{bmatrix}, \mathbf{R}_b^j = \begin{bmatrix} -0.6346 & -0.2806 & 0.7202 \\ -0.7727 & 0.2099 & -0.5991 \\ -0.0169 & 0.9366 & 0.3500 \end{bmatrix},$$

$$\mathbf{p}_b^j = \begin{bmatrix} -1.8290 \\ 1.2565 \\ 2.6285 \end{bmatrix}, \mathbf{R}_b^j = \begin{bmatrix} 0.4820 & 0.4467 & -0.7537 \\ 0.8761 & -0.2405 & 0.4178 \\ -0.0053 & 0.8617 & 0.5074 \end{bmatrix}.$$

REFERENCES

- [1] Bitcraze AB, “Crazyflie 2.0,” 2018, Accessed: March 2018. [Online]. Available: <https://www.bitcraze.io/crazyflie-2/>
- [2] M. Greiff, “Modelling and Control of the Crazyflie Quadrotor for Aggressive and Autonomous Flight by Optical Flow Driven State Estimation,” *Department of Automatic Control, Lund University, Sweden, MSc Thesis TFRT-6026 ISSN 0280-5316*, 2017.
- [3] HTC, “The VIVE Lighthouse System,” 2018, Accessed: March 2018. [Online]. Available: <https://www.vive.com/us/product/vive-virtual-reality-system/>
- [4] M. W. Mueller, M. Hehn, and R. D’Andrea, “Covariance Correction Step for Kalman Filtering with an Attitude,” *Journal of Guidance, Control, and Dynamics*, pp. 1–7, 2016.
- [5] M. W. Mueller, M. Hamer, and R. D’Andrea, “Fusing ultra-wideband range measurements with accelerometers and rate gyroscopes for quadcopter state estimation,” in *2015 IEEE International Conference on Robotics and Automation (ICRA)*, May 2015, pp. 1730–1736.
- [6] H. Chao, Y. Gu, and M. Napolitano, “A survey of optical flow techniques for robotics navigation applications,” *Journal of Intelligent & Robotic Systems*, vol. 73, no. 1-4, pp. 361–372, 2014.
- [7] R. J. Fontana, “Recent system applications of short-pulse ultra-wideband (UWB) technology,” *IEEE Transactions on microwave theory and techniques*, vol. 52, no. 9, pp. 2087–2104, 2004.
- [8] A. Ledergerber, M. Hamer, and R. D’Andrea, “A robot self-localization system using one-way ultra-wideband communication,” in *Intelligent Robots and Systems (IROS), 2015 IEEE/RSJ International Conference on*. IEEE, 2015, pp. 3131–3137.
- [9] E. Fresk, K. Ödmark, and G. Nikolakopoulos, “Ultra WideBand enabled Inertial Odometry for Generic Localization,” *IFAC-PapersOnLine*, vol. 50, no. 1, pp. 11465–11472, 2017.
- [10] S. K. Kay, *Fundamentals of Statistical Signal Processing: Estimation theory*. Englewood Cliffs, NJ, USA: Prentice-Hall, 1993.
- [11] O. Besson and Y. I. Abramovich, “On the Fisher information matrix for multivariate elliptically contoured distributions,” *IEEE Signal Processing Letters*, vol. 20, no. 11, pp. 1130–1133, 2013.
- [12] F. L. Markley, “Attitude error representations for Kalman filtering,” *Journal of guidance, control, and dynamics*, vol. 26, no. 2, pp. 311–317, 2003.
- [13] J. Sola, “Quaternion Kinematics for the error-state Kalman filter,” *arXiv preprint arXiv:1711.02508*, 2017.
- [14] R. M. Murray, Z. Li, and S. S. Sastry, *A mathematical introduction to robotic manipulation*. CRC press, 1994.
- [15] V. Semiconductors, “Bpw34 datasheet,” 2018, Accessed: March 2018. [Online]. Available: <https://www.mouser.se/ds/2/427/bpw34-240374.pdf>
- [16] G. S. Chirikjian, *Stochastic Models, Information Theory, and Lie Groups, Volume 2: Analytic Methods and Modern Applications*. Springer Science & Business Media, 2011, vol. 2.